Science Advances
AAAS

advances.sciencemag.org/cgi/content/full/7/2/eabc7885/DC1

Supplementary Materials for

Acoustohydrodynamic tweezers via spatial arrangement of streaming vortices

Haodong Zhu, Peiran Zhang, Zhanwei Zhong, Jianping Xia, Joseph Rich, John Mai, Xingyu Su, Zhenhua Tian, Hunter Bachman, Joseph Rufo, Yuyang Gu, Putong Kang, Krishnendu Chakrabarty, Thomas P. Witelski, Tony Jun Huang*

*Corresponding author. Email: tony.huang@duke.edu

Published 6 January 2021, *Sci. Adv.* **7**, eabc7885 (2021)
DOI: 10.1126/sciadv.abc7885

The PDF file includes:

Other Supplementary Material for this manuscript includes the following:

(available at advances.sciencemag.org/cgi/content/full/7/2/eabc7885/DC1)

Supplementary Note S1. Device setup

The main component of the tweezer platform is an array of PZTs (7 mm × 7 mm × 0.2 mm) arranged in a periodic, reciprocal pattern of alternating and mutually orthogonal rectangles. As all PZTs are of the same size, each PZT can either be the center of a unit when actuated or a piece of barrier when its adjacent unit is actuated. A printed circuit board (PCB) with carved rectangular slots sized at 7.2 mm × 1 mm is designed to constrain the pattern and serve as a base to stabilize the whole platform. 3D-printed joints containing narrow slots with a size of 7.1 mm × 0.22 mm are used to both prevent the PZT plates from tilting and to maintain electrical continuity with the PCB. Hard plastic plates of the same size of 7 mm × 7 mm × 0.2 mm are used as non-functional barriers surrounding the PZT units. This maintains the barrier geometry around individual units, as each functional unit needs eight pieces of barriers with the same size surrounding it. The assembly of each barrier is a three-step process (Fig. S1). When functional, the entire platform needs to be submerged into a carrier fluid, such as water or oil.

In this configuration, since there is no direct liquid-solid contact by the droplet, the diffusion of reagents is the main reason for potential contamination. The carrier fluid should have a high density to carry the droplet, high chemical stability, and low diffusion at the operating surface to maintain a low cross-contamination rate. Considering all these requirements, Fluorinert^{TM} FC-40 is an ideal carrier fluid and is used in our experiments. As a fluorinated oil which is widely applied in droplet microfluidics and liquid breathing experiments, Fluorinert^{TM} FC-40 is immiscible in water, chemically inert, and oxygen-permeable. These properties of the FC-40 oil expands the versatility of the platform to move different types of objects or bio-analytes (Fig. 1, E to H).

Supplementary Note S2. 3-D flow field numerical simulations

When actuated using an electrical signal, piezoelectric materials will generate bulk acoustic waves (BAW) with resonant frequencies related to their initial geometric characteristics. Specifically, when a free-moving rectangular, thin, piezoelectric plate with dimensions of 7 mm × 7 mm × 0.2 mm is actuated at its thickness mode at 11 MHz, a plane wave will be produced along the thickness direction, with the center part of the plate having the highest vibration amplitude. The sound field produced by each upright PZT is governed by the following acoustic wave equation (*36*, *41*),

$$\rho \frac{\partial^2 p(\mathbf{r},t)}{\partial t^2} = \rho c^2 \nabla^2 p(\mathbf{r},t) + b\nabla^2 \left[\frac{\partial p(\mathbf{r},t)}{\partial t} \right] \tag{S1}$$

Where $p(\mathbf{r},t)$ is the sound pressure produced by the upright PZT as a function of both the position vector **r** with the start point at the center of the upright PZT on the bottom plane, and time *t*; ρ is the fluid density, *c* is the sound speed in the carrier liquid, and the acoustic dissipation factor *b* is

$$b = \frac{4}{3}\eta + \eta' \tag{S2}$$

where η is the dynamic viscosity of the surrounding fluid, and the volumetric viscosity η' can be neglected under incompressible conditions. The sound pressure $p(\mathbf{r},t)$ is a time- harmonic quantity. If the center of the upright PZT is at a point $\mathbf{r}_0$, the pressure at a spatial point $\boldsymbol{\chi} = \begin{bmatrix} x & y & z \end{bmatrix}^T$ can be written in the form of (*42*, *43*)

$$p(\boldsymbol{\chi},t) = \mathrm{Re}\left\{ P(\boldsymbol{\chi}-\mathbf{r}_0) e^{-i\left[\omega t + \mathbf{k}\cdot(\boldsymbol{\chi}-\mathbf{r}_0)\right]} \right\} = P(\boldsymbol{\chi}-\mathbf{r}_0)\cos\left[\omega t + \mathbf{k}\cdot\left(\boldsymbol{\chi}-\mathbf{r}_0\right)\right] \tag{S3}$$

where $\mathbf{k}$ is the wave vector with $|\mathbf{k}| = 2\pi/\lambda$. As the wavelength that we use,

$$\lambda = 2\pi c/\omega = c/f = 640/11\times10^6 = 58.18\mu m \tag{S4}$$

which is much smaller than the size of PZT (*i.e.*, 7 mm), $P(\mathbf{r})$ can be considered as a pressure produced by a plane wave that is constrained to the upright PZT plane region and propagating only on the direction perpendicular to the upright PZT surface. According to Stokes' law of sound attenuation, $P(\mathbf{r})$ decreases exponentially along the propagation direction as (*44*)

$$P(\mathbf{r}) = P_0 e^{-\alpha d} = P_0 e^{-\frac{2\eta\omega^2}{3\rho c^3} d} \tag{S5}$$

where d is the distance of the point $\boldsymbol{\chi}$ to the transducer surface, and P_0 is the relative amplitude of vibration on a specific point on the PZT surface. Based on previous simulation results (29), we made a brief estimation of the pressure field generated by adding a Gaussian distribution originating from the point with the highest magnitude of vibration on the PZT surface. We pick the point of the highest magnitude of vibration at z = 3 mm above the fixed base and set the size-based decaying parameter to be 5×10^6 m^{-1}. Under experimental conditions, the characteristic attenuation distance d^* can be estimated as

$$d^* = \frac{1}{\alpha} = \frac{3\rho c^3}{2\eta\omega^2} \tag{S6}$$

which is much larger than the size of PZT and also the wave length λ. Thus, the amplitude $P(\mathbf{r})$ can be considered as a constant in the working area.

Similarly, the velocity vector $\mathbf{v}(\boldsymbol{\chi},t)$ produced by an acoustic transducer centered at the point $\mathbf{r}_0$ in the sound field can be calculated as (*42*)

$$\mathbf{v}(\boldsymbol{\chi},t) = \frac{i}{\rho\omega}\nabla p(\boldsymbol{\chi},t) = \mathbf{V}(\boldsymbol{\chi}-\mathbf{r}_0)\cos\left[\omega t - \mathbf{k}\cdot\left(\boldsymbol{\chi}-\mathbf{r}_0\right)\right] \tag{S7}$$

where **k** is the wave vector. The spatial gradient of the Reynolds stress tensor produced by a single acoustic transducer $\overline{\mathbf{F}}(\boldsymbol{\chi})$ can be calculated using time average (as expressed using $\langle\ \rangle$) as (*36*, *45–47*)

$$\overline{\mathbf{F}}(\boldsymbol{\chi}) = -\rho\nabla\cdot\left\langle \mathbf{v}(\boldsymbol{\chi},t)\mathbf{v}(\boldsymbol{\chi},t)\right\rangle \tag{S8}$$

The total mean pressure $\overline{p}(\boldsymbol{\chi})$ produced by a single acoustic transducer is computed by (*36*, *45*, *46*)

$$\overline{p}(\boldsymbol{\chi}) = -\frac{1}{2\rho c^2}\frac{B}{A}\left\langle\left[p(\boldsymbol{\chi},t)\right]^2\right\rangle + \rho g z + p_f \tag{S9}$$

where p_f is the pressure distribution generated by the flow field. The nonlinear time-averaged terms over one period in the Navier–Stokes equations result in body forces acting on the fluid (*48*). Thus, during the simulation, the net steady acoustic streaming actuated by multiple acoustic transducers satisfies the governing equation (*47*)

$$\rho\mathbf{u}(\boldsymbol{\chi})\cdot\nabla\mathbf{u}(\boldsymbol{\chi}) = \overline{\mathbf{F}}(\boldsymbol{\chi}) - \nabla\overline{p}(\boldsymbol{\chi}) + \eta\nabla^2\mathbf{u}(\boldsymbol{\chi}) \tag{S10}$$

The net steady acoustic streaming also needs to satisfy the continuity equation

$$\nabla\cdot\mathbf{u}(\boldsymbol{\chi}) = 0 \tag{S11}$$

We carry out numerical simulations of these governing equations (S10-11). For the simulation model, we can choose one unit with four half PZT plates in this study. The other three immobile plates act as non-slip walls. Around and above the submerged PZT plates, there is liquid for transferring acoustic streaming. We simplify this model by designing symmetric boundaries and then solve for the velocity field in liquid. We only consider a quarter of the unit (second quadrant in the *x*-*y* plane) for analysis and put the *x*-*y* center at the base of the vibrating plate (marked in red in Fig. 3) as the zero point. Fig. S3A is a schematic of the model. The four shaded parts are PZT plates but only one is vibrating. Other boundary conditions and the setup are also labeled. Once the velocity field of the quarter unit is obtained, the entire velocity field and the vorticity can be calculated based on symmetry.

Parameters used in the simulation are shown in Table S1.

Supplementary Note S3. A simplified model for flow field reconstruction

As mentioned in Fig. 2D, the simulation results show a steady vortex structure in the flow field surrounding an upright PZT unit. To analyze the flow induced by the six vortex segments created by acoustic streaming, we make some simplifying assumptions about the flow field. The oil-air interface is considered to be a well-defined smooth surface, and all vortex segments are considered line segments. For a single vortex tube at a fixed size *a*, the vortex circulation strength $\Gamma(a)$ can be estimated as

$$\Gamma(a) = \iint_A (\nabla\times\mathbf{u})\cdot\mathbf{dA} \approx const\ \ (when\ \left|\tilde{\mathbf{r}}\right| > a) \tag{S12}$$

Based on the simulation results, the vortex has a finite spatial size that can be seen as a tube with radius a, the vorticity inside/outside the vortex tube at distance $\tilde{\mathbf{r}}$ can be estimated as

$$\left|\boldsymbol{\omega}(\tilde{\mathbf{r}})\right| \propto 1/\left|\tilde{\mathbf{r}}\right| \tag{S13}$$

$$\Gamma(\tilde{\mathbf{r}}) = \begin{cases} \Gamma_a a/\left|\tilde{\mathbf{r}}\right|, \left|\tilde{\mathbf{r}}\right| < a \\ \Gamma_a, \qquad \left|\tilde{\mathbf{r}}\right| \geq a \end{cases} \tag{S14}$$

The circulation of a single vortex unit Γ_a can be estimated by fitting to the numerical results of vorticity field (from Note S2). According to the Biot-Savart Law, the induced speed of a unit vortex tube with a circulation Γ and length **dl** to a specific point in the area is (*49*)

$$\mathbf{du} = \frac{\Gamma}{4\pi}\frac{\mathbf{dl}\times\tilde{\mathbf{r}}}{\left|\tilde{\mathbf{r}}\right|^3} \tag{S15}$$

Then we can integrate, along a line segment, the induced speed $\mathbf{du}_i$ of a vortex tube to a specific point $\boldsymbol{\chi}$ in the area. When Γ remains the same along the i^{th} vortex line placed at $\mathbf{l}_i = \overrightarrow{A_iB_i} = \mathbf{s}_{2,i} - \mathbf{s}_{1,i}$, the amplitude of this integrated speed is

$$\left|\mathbf{u}_i(\boldsymbol{\chi})\right| = \left|\int_{A_i}^{B_i}\mathbf{du}_i\right| = \frac{\Gamma_i}{4\pi}\int_{A_i}^{B_i}\frac{\sin\theta d\theta}{R_i(\boldsymbol{\chi})} = \frac{\Gamma_i}{4\pi R_i(\boldsymbol{\chi})}\left(\cos\theta_{1,i} - \cos\theta_{2,i}\right) \tag{S16}$$

in which the direction of $\mathbf{u}_i$, which can be expressed as $\mathbf{l}_i\times\mathbf{e}_i/\left|\mathbf{l}_i\right|$, is perpendicular to $\mathbf{e}_i$, the unit vector of the angular bisector of the two lines connecting the specific point $\boldsymbol{\chi}$ and two ends of the line segment. From the unit construction we have (Fig. 1B)

$$R_i(\boldsymbol{\chi}) = \left|\frac{\mathbf{l}_i}{\left|\mathbf{l}_i\right|}\times\left(\boldsymbol{\chi}-\mathbf{s}_{1,i}\right)\right| = \left|\frac{\mathbf{l}_i}{\left|\mathbf{l}_i\right|}\times\left(\boldsymbol{\chi}-\mathbf{s}_{2,i}\right)\right| = \frac{\left|\mathbf{l}_i\times\boldsymbol{\chi}-\mathbf{s}_{2,i}\times\mathbf{s}_{1,i}\right|}{\left|\mathbf{l}_i\right|} \tag{S17}$$

$$\cos\theta_{1,i} - \cos\theta_{2,i} = \frac{\left(\boldsymbol{\chi}-\mathbf{s}_{1,i}\right)\cdot\mathbf{l}_i}{\left|\boldsymbol{\chi}-\mathbf{s}_{1,i}\right|\left|\mathbf{l}_i\right|} - \frac{\left(\boldsymbol{\chi}-\mathbf{s}_{2,i}\right)\cdot\mathbf{l}_i}{\left|\boldsymbol{\chi}-\mathbf{s}_{2,i}\right|\left|\mathbf{l}_i\right|} \tag{S18}$$

$$\mathbf{e}_i = \frac{1}{2}\left(\frac{\left(\boldsymbol{\chi}-\mathbf{s}_{1,i}\right)}{\left|\boldsymbol{\chi}-\mathbf{s}_{1,i}\right|} + \frac{\left(\boldsymbol{\chi}-\mathbf{s}_{2,i}\right)}{\left|\boldsymbol{\chi}-\mathbf{s}_{2,i}\right|}\right) \tag{S19}$$

by substituting into the formula (S16) we can get

$$\mathbf{u}_i(\boldsymbol{\chi}) = \frac{\Gamma_i}{8\pi\left|\mathbf{l}_i\times\boldsymbol{\chi}-\mathbf{s}_{2,i}\times\mathbf{s}_{1,i}\right|}\left[\frac{\left(\boldsymbol{\chi}-\mathbf{s}_{1,i}\right)\cdot\mathbf{l}_\mathbf{i}}{\left|\boldsymbol{\chi}-\mathbf{s}_{1,i}\right|\left|\mathbf{l}_\mathbf{i}\right|} - \frac{\left(\boldsymbol{\chi}-\mathbf{s}_{2,i}\right)\cdot\mathbf{l}_i}{\left|\boldsymbol{\chi}-\mathbf{s}_{2,i}\right|\left|\mathbf{l}_i\right|}\right]\mathbf{l}_i\times\left[\frac{\left(\boldsymbol{\chi}-\mathbf{s}_{1,i}\right)}{\left|\boldsymbol{\chi}-\mathbf{s}_{1,i}\right|} + \frac{\left(\boldsymbol{\chi}-\mathbf{s}_{2,i}\right)}{\left|\boldsymbol{\chi}-\mathbf{s}_{2,i}\right|}\right] \tag{S20}$$

with all $\mathbf{s}_{1,i}$ and $\mathbf{s}_{2,i}$ as fitted values based on the simulation results. Finally, to preserve the boundary condition where there is no flux on the operating surface, six mirrored vortex segments according to the operating surface are also considered and added up as a final estimation of the induced speed of the shaped acoustic streaming created by a single, actuated, upright, PZT unit, so 12 pieces of the vortex tubes are considered in total:

$$\mathbf{u}(\boldsymbol{\chi}) = \sum_{i=1}^{12} \mathbf{u}_i(\boldsymbol{\chi}) = \sum_{i=1}^{12} \frac{\Gamma_i}{4\pi R_i(\boldsymbol{\chi})} \left(\cos\theta_{1,i} - \cos\theta_{2,i}\right) \frac{\mathbf{l}_i}{|\mathbf{l}_i|} \times \mathbf{e}_i \tag{S21}$$

The effect of the barriers near the induced vortex tube pairs can be used to further correct for the derived $\mathbf{u}(\boldsymbol{\chi})$, which can be expressed as a combination of the vortex tube and its decaying mirror images along with the surrounding barriers:

$$\tilde{\mathbf{u}}(\boldsymbol{\chi}) = \mathbf{u}(\boldsymbol{\chi}) + \sum_{n=1}^{N} \sum_{m=0}^{n-1} \sum_{k=0}^{3} \mathbf{u}(\boldsymbol{\chi}_{m,n,k}) \gamma^n \tag{S22}$$

with

$$\boldsymbol{\chi}_{m,n,k} = \boldsymbol{\chi} - 2mL\left(\cos\frac{k\pi}{2}\mathbf{e}_x + \sin\frac{k\pi}{2}\mathbf{e}_y\right) - 2(n-m)L\left(\cos\frac{k\pi}{2}\mathbf{e}_y - \sin\frac{k\pi}{2}\mathbf{e}_x\right) \tag{S23}$$

where $\mathbf{u}(\boldsymbol{\chi}_{m,n,k})$ is the mirror image of the flow induced by one of the four surrounding half barriers by reflection n times, L = 6 mm is the x and y extents of a quarter unit, $\mathbf{e}_x$ and $\mathbf{e}_y$ are the unit vector along x and y-axis respectively, and γ is a decay parameter. In the COMSOL interface, we selected the values $N = 3$, $\gamma = 0.1$.

Supplementary Note S4. Multi-unit actuation and fluid field superposition

According to the superposition principle that is valid for different sound fields actuated by multiple acoustic transducers (*37*), the total time-harmonic acoustic quantities of N different units can be written as:

$$p^{total}(\boldsymbol{\chi}, t) = \sum_{n=1}^{N} p_k(\boldsymbol{\chi}, t) = \sum_{n=1}^{N} P_n(\boldsymbol{\chi} - \mathbf{r}_{0,n}) \cos\left[\omega t - \mathbf{k}_n \cdot \left(\boldsymbol{\chi} - \mathbf{r}_{0,n}\right)\right] \tag{S24}$$

and

$$\mathbf{v}^{total}(\boldsymbol{\chi}, t) = \frac{i}{\rho\omega} \nabla p^{total}(\boldsymbol{\chi}, t) = \sum_{n=1}^{N} \mathbf{v}_k(\boldsymbol{\chi}, t) = \sum_{n=1}^{N} \mathbf{V}_n(\boldsymbol{\chi} - \mathbf{r}_{0,n}) \cos\left[\omega t - \mathbf{k}_n \cdot \left(\boldsymbol{\chi} - \mathbf{r}_{0,n}\right)\right] \tag{S25}$$

Similarly, we can get the total force generated for multi-unit actuation

$$\overline{\mathbf{F}}^{total}(\boldsymbol{\chi}) = -\rho\nabla\cdot\left\langle \mathbf{v}^{total}(\boldsymbol{\chi},t)\mathbf{v}^{total}(\boldsymbol{\chi},t)\right\rangle \tag{S26}$$

$$\overline{p}^{total}(\boldsymbol{\chi}) = -\frac{1}{2\rho c^2}\frac{B}{A}\left\langle\left[p^{total}(\boldsymbol{\chi},t)\right]^2\right\rangle + \rho g z + p_f \tag{S27}$$

and the governing equation for the combined force

$$\rho\left(\mathbf{u}^{total}(\boldsymbol{\chi})\cdot\nabla\right)\mathbf{u}^{total}(\boldsymbol{\chi}) = \overline{\mathbf{F}}^{total}(\boldsymbol{\chi}) - \nabla\overline{p}^{total}(\boldsymbol{\chi}) + \eta\nabla^2\mathbf{u}^{total}(\boldsymbol{\chi}) \tag{S28}$$

Based on the approximation of the Reynolds number discussed in the article, which is $\mathrm{Re}\approx\rho u^* D^*/\eta = 1.91$, the system can still be considered as a Stokes flow system, which retains the linear properties in the governing equation. So, for multi-unit actuation situations, the flow field generated by a combination of *N* units is:

$$\mathbf{u}_{comb}(\boldsymbol{\chi}) \approx \sum_{n=1}^{N}\mathbf{u}_k^*(\boldsymbol{\chi}) = \sum_{n=1}^{N}\frac{\Gamma_n}{\Gamma_0}\left[L_n\left(x_{0,n},y_{0,n}\right)\right]\mathbf{u}(x-x_{0,n},y-y_{0,n},z) \tag{S29}$$

where Γ_n/Γ_0 is a dimensionless indicator of vortex circulation of each separate unit, and $\left(x_{0,n},y_{0,n}\right)$ is the center of the n^{th} unit in the *x*-*y* plane. $\left[L_n\left(x_{0,n},y_{0,n}\right)\right]$ is a transformation matrix parameter based on the overlapping of vortices in the region and the orientation of the upright PZT unit. The effect of $\left[L_n\left(x_{0,n},y_{0,n}\right)\right]$ can be expressed as

$$\begin{aligned}\left[L_n\left(x_{0,n},y_{0,n}\right)\right]\mathbf{u}\left(x,y,z\right) &= \left[L_n\left(x_{0,n},y_{0,n}\right)\right]\begin{bmatrix}u & v & w\end{bmatrix}^T \\ &= \begin{cases}\begin{bmatrix}v & u & w\end{bmatrix}^T_{(y-y_{0,n}+x_{0,n},x+y_{0,n}-x_{0,n},z)} & when\ n^{th}\ unit\ \perp\ the\ first\ one \\ \begin{bmatrix}u & v & w\end{bmatrix}^T_{(x,y,z)} & when\ n^{th}\ unit\ //\ the\ first\ one\end{cases}\end{aligned} \tag{S30}$$

Supplementary Note S5. Optimization of system parameters

To design the vertical PZT unit structure in the AHT system, two steps are needed: the optimized combination of system parameters to create the stable vortex pairs, and the vortex-based simplification to predict the flow field and the position of the hydrodynamic trap. More specifically, we want the vortex pairs generated to be strong and condense, and also at the right place to realize omnidirectional attracting on the operating surface (*i.e.*, $z = H$).

We believe the reciprocal pattern of the PZT units is a key point to realize the stable manipulation effect. Thus, for optimization of the system, we will always keep the unit pattern identical to what it is in the paper. Meanwhile, the adjustable system parameters mainly include the dimension of the system (*i.e.*,

the size of a unit), the distance between units, the thickness of the PZT plate (*i.e.*, the frequency of acoustic input applied) and the height of the FC-40 oil layer. We will discuss the effect of each of these parameters point-by-point.

The effect of dimensions: Based on the inherent linearity of governing equation under low Reynolds number conditions, the performance of the AHT system will not change with the scale. Meanwhile, simulation results also show that the system will preserve the same performance when the whole system is scaled down. For example, we can consider the flow field result on the operating surface on a quarter unit with all the geometric scale (including the size and shape of PZT unit) decreased to 50% of their original value. While the system is universally scaled, the flow pattern within the quarter unit will also scale with geometric size but the shape will be the same. With the pressure input level unchanged, the magnitude of velocity will be 2-1/2 times of the original one.

The effect of distance between units: The distance between centers of adjacent units in the pattern, ΔL, is an important system parameter to create a stable hydrodynamic trap above a unit. ΔL determines both the strength and the position of vortex pairs generated in the area of $0 < z < 5$ mm. Here we use the coordinates from Fig. 2 in the paper, keep $H = 8$ mm, and use the x-y intersection of the vorticity field at $z = 2.5$ mm to illustrate the effect of ΔL on vortex generation. Three example intersections of the vorticity field (including the condition in the paper, $\Delta L = 6$ mm) are listed in Fig. S4, A-C. To compare the performance of different designs, we also use the criteria including:

1) Position of the vortex tube: the position of the point with the maximum magnitude of vorticity in the area. The x position of the center of all vortex tubes are always close to $x = -3.5$ mm because of Kelvin-Helmholtz instability. On the other hand, the y position will shift with different ΔL;

2) Strength of the vortex tube: the maximum magnitude of vorticity in the area;

3) Size of the vortex tube: the average full width at half maximum (FWHM) of the magnitude of vorticity in the area;

4) Stability of hydrodynamic trapping: flow speed at two points on the border of the unit, *i.e.* u_x at $(x, y, z) = (\Delta L, 0, H)$ for longitudinal mode and u_y at $(x, y, z) = (0, \Delta L, H)$ for lateral mode.

Based on the results from Fig. S4, the strength of vortex generated will reach a stable level after ΔL reaches 5 mm, while both the size and the y-position of the vortex tube keeps increasing as ΔL increases. Though the attracting ability remains in the x-direction, the system loses attracting stability in the y-direction when $\Delta L > 7$ mm. Considering all the results mentioned above, we can pick ΔL with the range of $5 \text{ mm} < \Delta L < 7$ mm for further optimization, and $\Delta L = 6$ mm is a reasonable choice for the AHT prototype build in the paper.

The effect of thickness of the PZT plate: According to equation S8 in the supplementary materials section, the effect of body force produced by acoustic pressure is a time-averaged effect. Meanwhile,

the thickness of the PZT plate is directly proportional to the wavelength when the PZT is actuated in bending mode. Thus, as long as the size of the PZT is much larger than the wavelength, the performance of the system will not be affected.

The effect of the height of the FC-40 oil layer: The height of the oil layer is another important system parameter that affects the performance of the system. The height of the oil layer mainly determines the upper limit of the object size being manipulated. Basically, the radius (or half of the longer orbits) of the object should not exceed the depth of the oil layer, since if the object gets too large and can contact with the vibrating PZT unit, it will likely get stuck on the PZT structures.

The height of the oil layer also affects the vortex tube in the region of 5 mm < z < H. We use the similar approach used in analyzing the effect of ΔL to analyze the effect of H when ΔL is set to 6 mm. We choose the y-z intersection of the vorticity field at x = -1 mm, and plot the position, strength, and size of the vortex tube and flow speed at two points on the border of the unit with different H respectively (Fig. S5).

The results from Fig. S5 agrees well with Fig. S4 on the y-position, strength, and size of the vortex tube. The result also shows that the vortex tube is less affected by H than ΔL. However, when H is too small the vortex tube tends to extend in the y-direction and make the vortex-based simplification less accurate when calculating the flow field. A reasonable range for the future optimization of H would be H > 7 mm. Based on the discussion above, the system parameters were chosen in the paper (ΔL = 6 mm, H = 8 mm) and are reasonably optimized for the prototype.

Supplementary Note S6. Measurement of the radial velocity profile

We use a video recording at 25 fps to capture the movement of 30 μm diameter microparticles near the center and process the video with a C++ code that can handle traces from a massive number of particles. As the density of the particles (1.9×10^3 kg/m^3) is similar to FC-40 oil (1.855×10^3 kg/m^3), they can be suspended in the oil for longer than 20 minutes, which meets the needs for observation. The particles mainly move along streamlines under the influence of the drag force, so we can predict the flow field at a given x-y intersection with $z \in (0, H]$ based on stacked time-elapsed images of their path lines. (Fig. S6A).

Supplementary Note S7. Droplet tracing

For demonstration experiments, we use a fast camera to capture the movement of a droplet at 30 fps and maintain the single unit actuation voltage at 8 Vpp. We then use a MATLAB program for image processing and calculating the droplet speed.

The method used for droplet speed calculation is mentioned in Fig. 4B. Summarizing, we alternate actuation in the longitudinal mode and lateral mode to move the target drop of a given size back and forth five times to obtain the average motion in the longitudinal and lateral modes. We use the average speed between the set thresholds under specific [*H, D*] conditions as a data point used in the color map in Fig. 4., F and G.

Supplementary Note S8. Theoretical estimation of droplet/particle movement

After obtaining the estimated flow field function $\mathbf{u}(\boldsymbol{\chi})$, we can further build a model based on the flow around a droplet of a given size. The floating droplet will mainly experience four forces: the Stokes drag force $\mathbf{F}_d$, the acoustic radiation force on the *x*-*y* plane, and the buoyancy force which is equal to the gravitational force in the *z*-direction. (The drag force in the *z*-direction is neglected because the acceleration caused by $\mathbf{F}_d$ is much smaller than *g*, which will not cause a significant change in the overlapping surface of the droplet with the oil layer). Based on Stokes' law for a spherical object in a uniform flow field, the shear stress on a droplet, per unit area, with a radius *R=D/2* can be estimated as

$$\boldsymbol{\sigma} = \frac{3\eta\left(\mathbf{u}-\mathbf{u}_d\right)}{2R} \tag{S31}$$

Then we can integrate this force on the part of the floating droplet that interacts with the FC-40 oil. As shown in Fig. S7, the position of a small surface unit of the interaction region between the droplet and oil can be expressed as

$$\tilde{\boldsymbol{\chi}}\left(x,y,R,\theta,\varphi\right) = \left[x+R\cos\theta\sin\varphi \quad y+R\sin\theta\sin\varphi \quad H-R\cos\varphi+R\cos\varphi_0\right]^T \tag{S32}$$

and the total drag force yields

$$\mathbf{F}_d = \oiint_{\Omega_s,\varphi\le\varphi_0}\boldsymbol{\sigma}dS = \oiint_{\Omega_s,\varphi\le\varphi_0}\frac{3\eta}{2R}\left[\mathbf{u}\left(\tilde{\boldsymbol{\chi}}\right)-\mathbf{u}_d\right]\left(R^2 d\theta d\varphi\right) \tag{S33}$$

so, the acceleration of the droplet is

$$\mathbf{a}_d = \frac{d^2\mathbf{s}_d}{dt^2} = \frac{\mathbf{F}_d}{m} = \frac{3\mathbf{F}_d}{4\rho_d\pi R^3} \tag{S34}$$

Then we can use a MATLAB code based on the Gauss-Seidel method to iterate the trace of the droplet with a starting velocity of the droplet $\mathbf{u}_d\big|_{t=0} = 0$ which can start at any point in the area. In the code, the angle of the step is set as $\pi/50$ deg, and the time step *dt* is set as 1×10^{-3} *s*. The calculated average velocity based on a combination of system parameters [*D, H*] is used to generate a data point in Fig. 4., H and I, which is similar to the corresponding value from the experimental results

Supplementary Note S9. Programmable control system setup

The automated AHT platform is shown in Fig. S8. First, the sequencing graph of the specific function (*i.e.* merging, routing, etc.) is loaded into the computer. Next, the synthesizer software takes this sequencing graph as an input and generates the schedule of fluidic operations with respect to the location of PZT plates and hydrodynamic traps. Finally, the synthesis result is translated into a 0/1 sequence (or pattern) and loaded into the registers on the prototype. A combination of a signal generator and an amplifier generates a signal (*e.g.*, 11 MHz and 8 Vpp) that can activate the upright PZTs. The 0/1 bits loaded into the registers are used to control the ON/OFF state of the switches, and thus control the ON/OFF state of each upright PZT on the prototype platform. Therefore, by applying an appropriate programmed binary pattern to the registers, it can carry out automated fluidic operations and bioassays on the prototype platform.

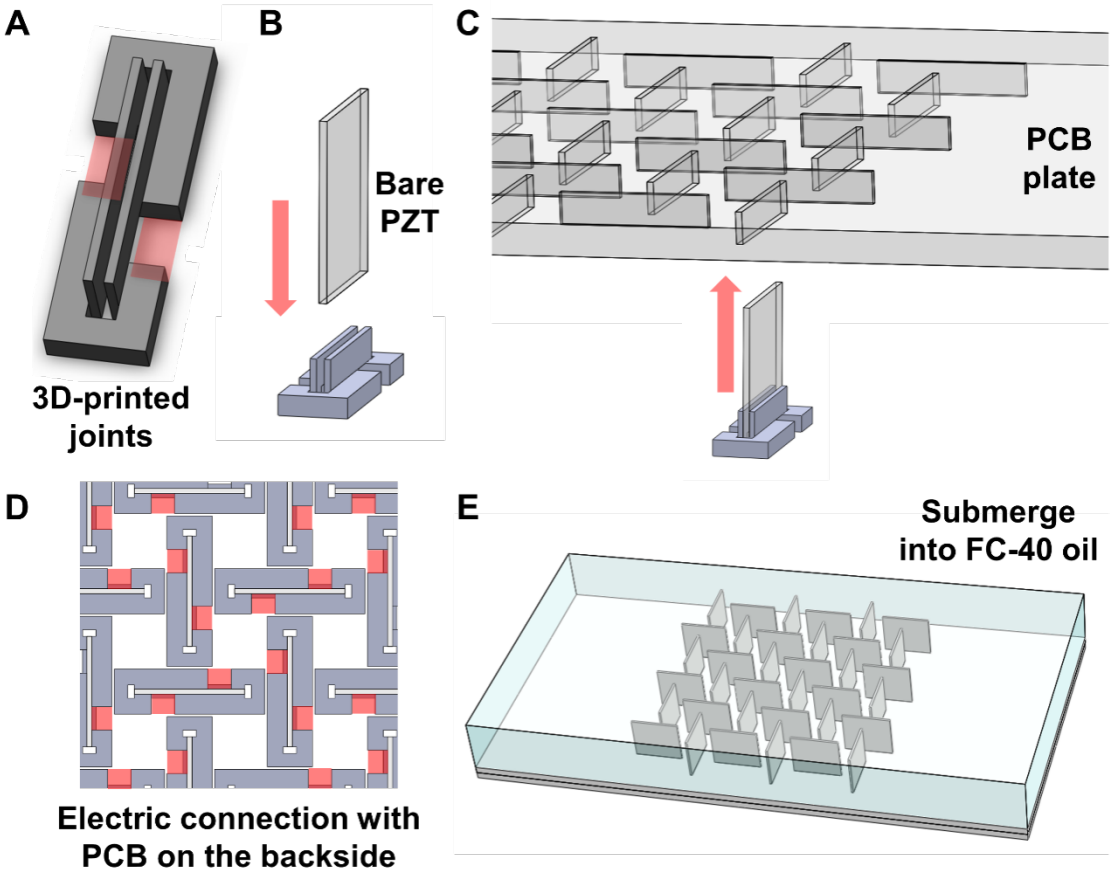

Fig. S1. Three-step fabrication approach for the prototype. The 16-unit AHT prototype has a simple three-step fabrication process. (**A** to **B**) First, a 3-D printed joint (with the red shaded part as a blank spacer for later electrical connections) is attached to the PZT plate to set it upright. (**C**) Then the upright PZTs are plugged in the pre-cut slots on the PCB base plate. (**D**) The whole prototype is then stabilized using silver epoxy to fill the blank spacer area from the backside. (**E**) Finally, the prototype in submerged into FC-40 oil and is ready to use.

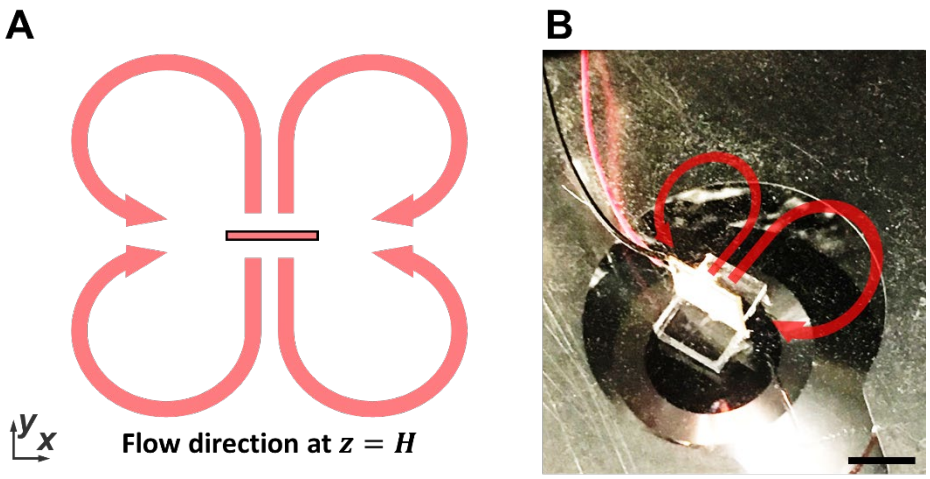

Fig. S2. Flow generated by vibrating a bare plate. (**A**) A sketch of the symmetric flow pattern generated on the operating surface ($z = H$) by vibrating an upright PZT plate submerged in FC-40 oil The liquid is pushed away in the vibrating direction (*i.e.*, the *y*-axis in this orientation) and returns from the other direction (*i.e.*, the *x*-axis in this image), forming a "clover" shape. (**B**) Preliminary results from a bare PZT plate that is fixed with PDMS in the bottom and actuated in FC-40 oil. 30 μm silver microparticles are added to one side of it to show the flow pattern. Suspended microparticles form two lobes of the "clover" shape on the oil surface, but the flow field is not perfectly symmetric due to the impedance caused by the presence of the wire connection point on the upper-left corner. The scale bar is 5 mm. Photo Credit: Haodong Zhu, Duke University.

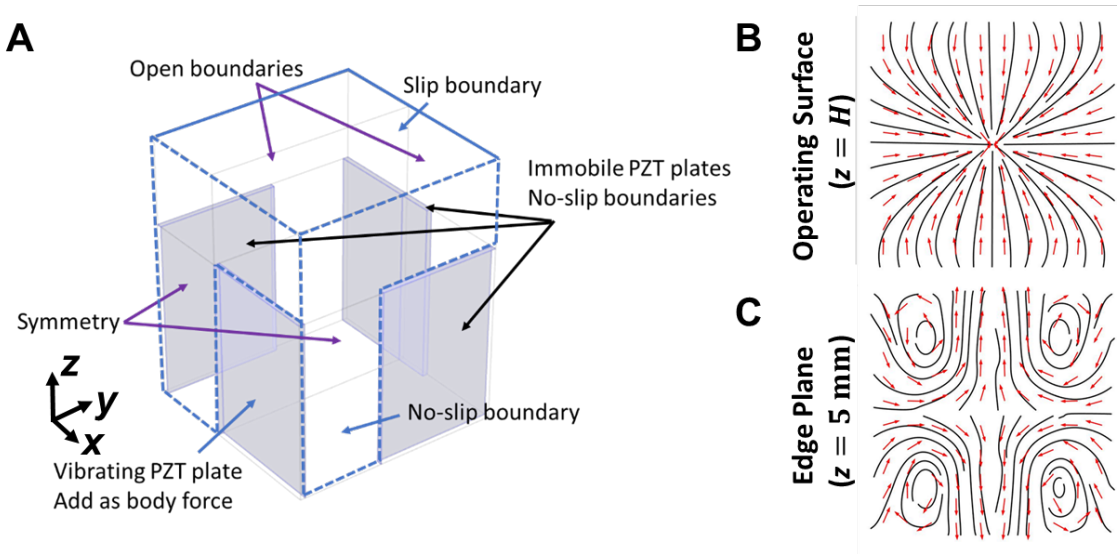

Fig. S3. Simulation results for the quarter unit model. (**A**) Model of the quarter unit with an illustration of the applied boundary conditions. The four shaded parts are half PZT plates. All other parts including the regions above the plates are filled with FC-40 oil. Blue arrows point at vibrating solid boundaries, and also indicate both the top and bottom boundaries. Black arrows point at static solid boundaries. Purple arrows point at all other open boundaries, including two symmetric boundaries due to the geometry of the quarter unit. (**B** and **C**) Flow field simulation results from a single unit actuation at the operating surface ($z = H$, B) and the edge plane ($z = 5$ mm, C). The scale is the same in Fig. 2, E to L.

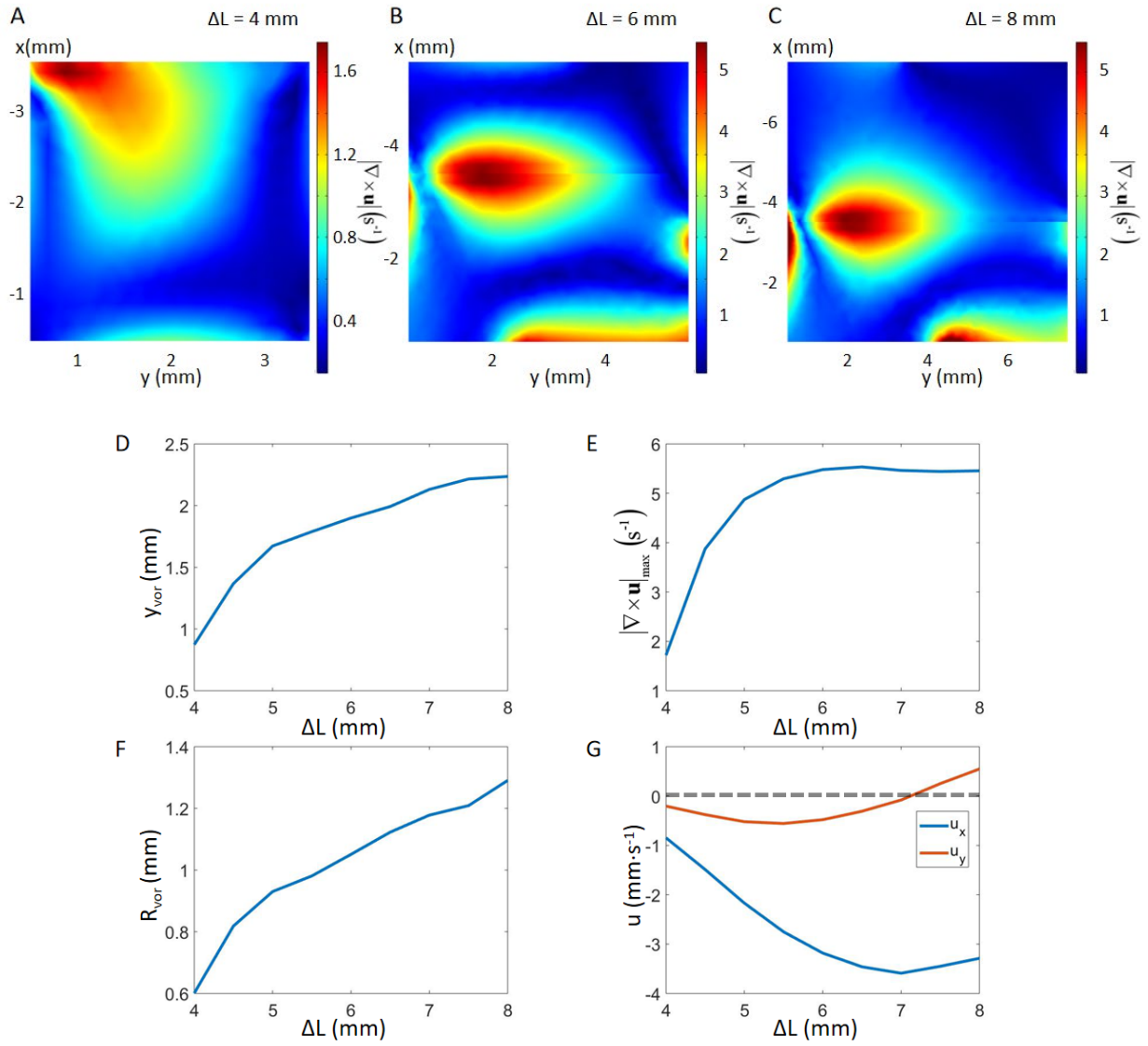

Fig. S4. The influence of *ΔL*, the distance between units on the performance of the system when *H* = 8 mm. (**A** to **C**) Intersections of the vorticity field under different Δ*L*. (**D**) The relation of the center position of the vortex tube, y_{vor} with different Δ*L*. (**E**) The relation of the maximum magnitude of vorticity with different Δ*L*. (**F**) The relation of the size of the vortex tube, R_{vor},with different Δ*L*. (**G**) The relation of flow velocity at two border points of the unit with different Δ*L*. The trapping behavior only occurs when velocity in both directions (*i.e.*, both u_x and u_y) are negative, suggesting that the system loses attracting stability in *y*-direction when Δ*L* > 7 mm.

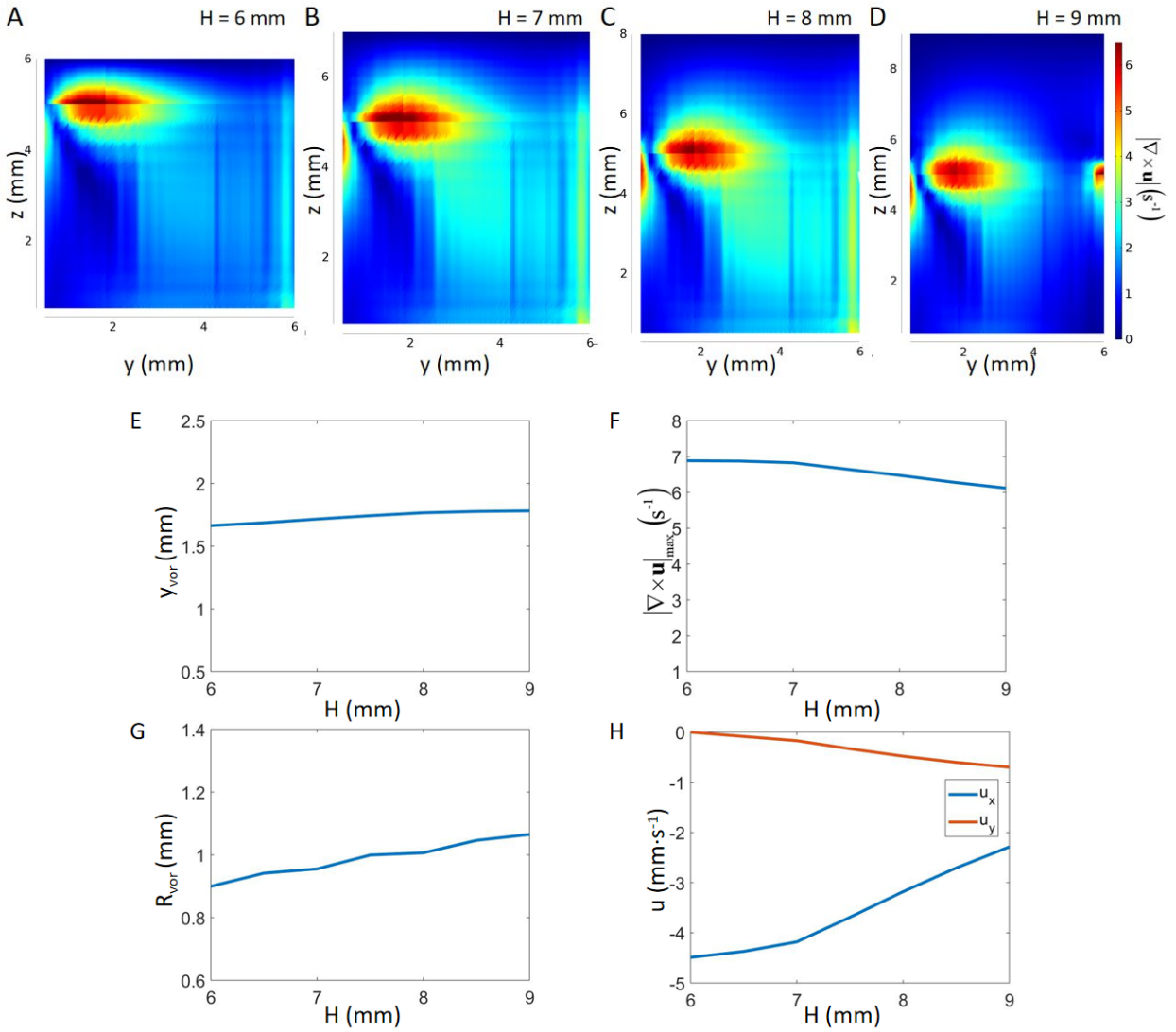

Fig. S5. The influence of *H*, the height of the oil layer on the performance of the system when *ΔL* = 6 mm. (**A** to **D**) Intersections of vorticity fields under different *H*. (**E**) The relation of the center position of the vortex tube, y_{vor},with different *H*. (**F**) The relation of the maximum magnitude of vorticity with different *H*. (**G**) The relation of the size of the vortex tube, R_{vor}, with different *H*. (**H**) The relation of flow velocity at two border points of the unit with different *H*.

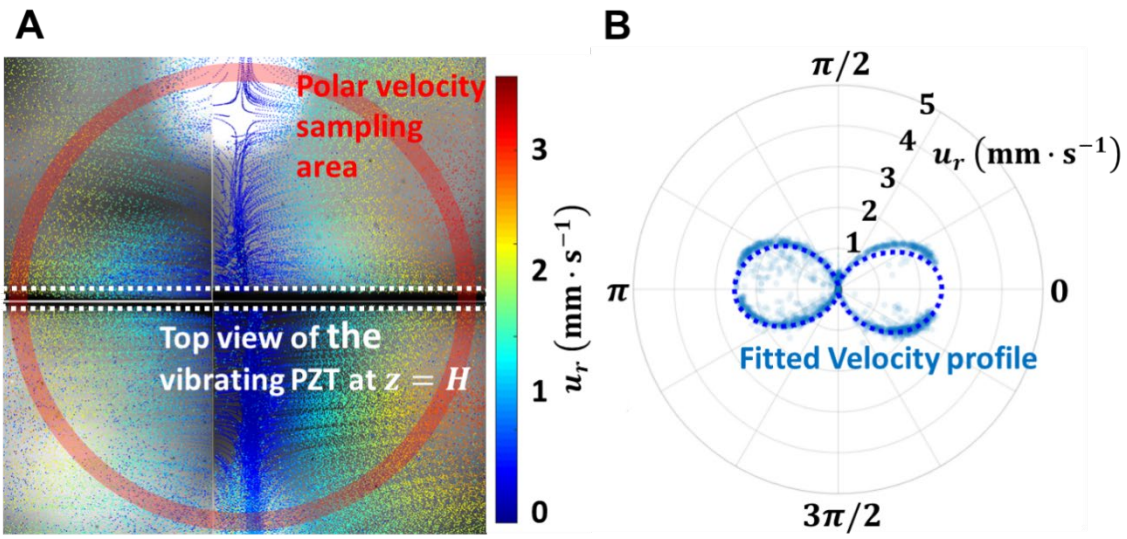

Fig. S6. Measurement method of the radial velocity profile around the attraction point. (**A**) Processed experimental result of the particle trace near the hydrodynamic trapping point as shown in Fig. 2A, with the same region size (7 mm × 7 mm) as in Fig. 2, D, G, J, and L. The color in the background represents the velocity of the detected single particle and its motion trace, respectively. The red circle shows the recording area for the radial velocity calculation. The scale bar is 1 mm. (**B**) The corresponding radial velocity profile as obtained from Fig. S6A. The dotted line is a fitted curve based on a scatter plot of the average velocity of each detected particle as it passed through the sampling area. This curved fit shows that the main flow pattern on the operating surface ($z = H$) is attracting in the ± x-direction. Photo Credit: Haodong Zhu, Duke University.

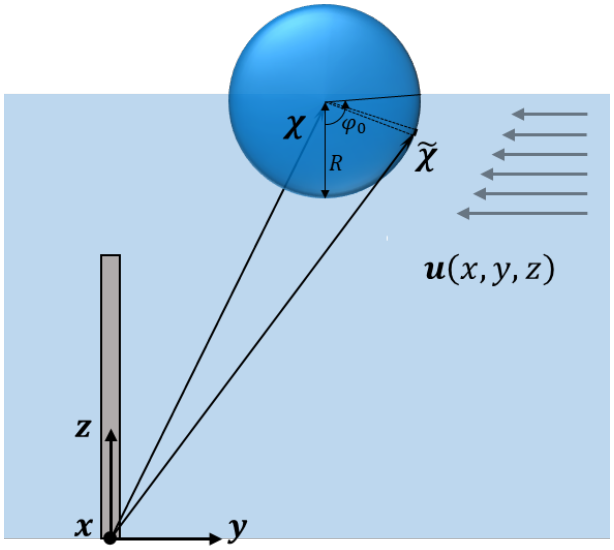

Fig. S7. Schematic of the simplified flow field and droplet interaction. $\tilde{\chi}$ represents the position of a small surface unit on the interaction region of a droplet centered at a position χ located in polar coordinates. The total drag force is estimated by integrating the Stokes drag force, per unit area, across all the small surface units on the interaction region

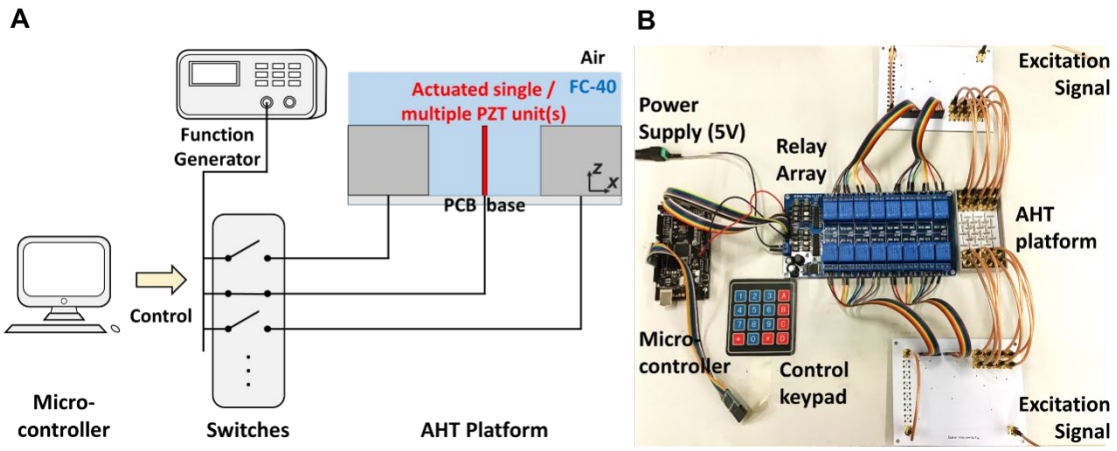

Fig. S8. The control system for programmable droplet tracing. (**A**) Illustrative diagram of the proposed control system. (**B**) Experimental setup for the proposed control system, which contains a micro-controller, a relay array as the switches, and an AHT platform. A combination of a function generator and an amplifier generates the excitation signal. Photo Credit: Haodong Zhu, Duke University.

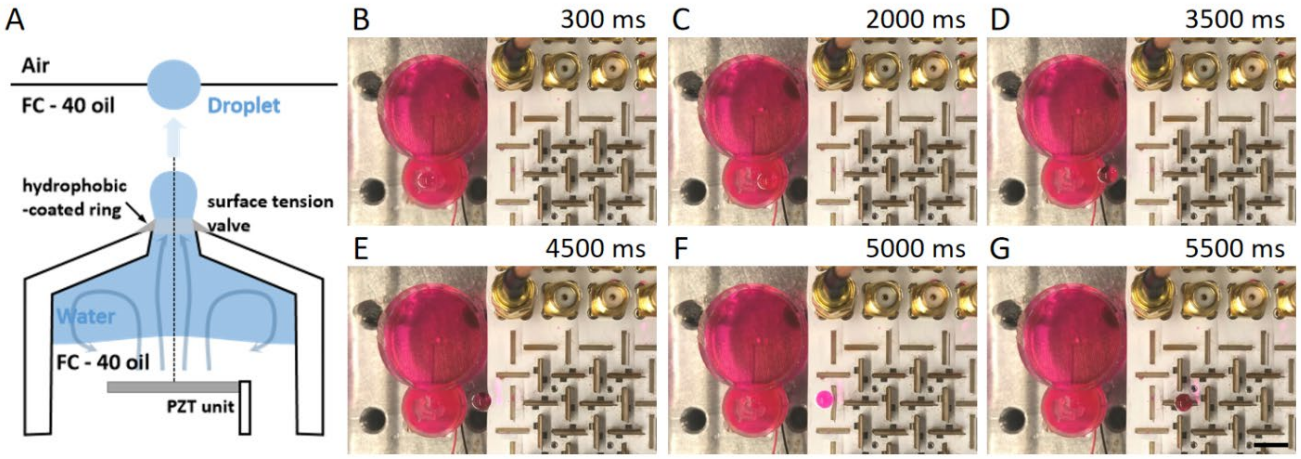

Fig. S9. The AHT prototype integrated with a droplet generator. (**A**) The design of the droplet generator in the FC-40 oil with the water sealed in the cartridge with hydrophobic ring coated on top. A PZT unit (same as the ones used in the AHT array) is set underneath the water layer. When actuated with a 300 ms electric pulse at 210 Vpp, the PZT unit bends and generates a flow jet that pushes the aqueous fluid against the surface tension valve and creates a droplet to float to the operating surface. (**B** to **G**) Snapshots from different time frames to show the creation of a droplet and its movement to the AHT platform. The water is colored with Rhodamine B (140 mg/L). The attracting unit on the AHT platform works at 30 Vpp. The scale bar is 7 mm. Photo Credit: Haodong Zhu, Duke University.

b	4.5×10^{-3} Pa·s	P_0	18000 Pa	c	640 m·s^{-1}
ω	6.9115×10^{7} s^{-1}	η	3.4×10^{-3} Pa·s	ρ	1855 kg·m^{-3}
α	22.27 m^{-1}	$\Gamma(a)$	6×10^{-6} m^{2}·s^{-1}	g	9.81 m·s^{-2}
B/A	3	ρ_d	1000 kg·m^{-3}	γ	0.1
dt	0.001 s	$d\theta$	$\pi/50$	$d\varphi$	$\pi/50$

Table S1. Parameters used in numerical simulations and for the simplified model.

REFERENCES AND NOTES

1. M. L. Juan, M. Righini, R. Quidant, Plasmon nano-optical tweezers. *Nat. Photonics* **5**, 349–356 (2011).
2. K. Choi, A. H. C. Ng, R. Fobel, A. R. Wheeler, Digital microfluidics. *Annu. Rev. Anal. Chem.* **5**, 413–440 (2012).
3. S. K. Cho, H. Moon, C.-J. Kim, Creating, transporting, cutting, and merging liquid droplets by electrowetting-based actuation for digital microfluidic circuits. *J. Microelectromech. Syst.* **12**, 70–80 (2003).
4. J. Lee, H. Moon, J. Fowler, T. Schoellhammer, C.-J. Kim, Electrowetting and electrowetting-on-dielectric for microscale liquid handling. *Sensors Actuators A Phys.* **95**, 259–268 (2002).
5. M. G. Pollack, R. B. Fair, A. D. Shenderov, Electrowetting-based actuation of liquid droplets for microfluidic applications. *Appl. Phys. Lett.* **77**, 1725–1726 (2000).
6. P. K. Wong, T.-H. Wang, J. H. Deval, C.-M. Ho, Electrokinetics in micro devices for biotechnology applications. *IEEE/ASME Trans. Mechatron.* **9**, 366–376 (2004).
7. N. Francois, H. Xia, H. Punzmann, P. W. Fontana, M. Shats, Wave-based liquid-interface metamaterials. *Nat. Commun.* **8**, 14325 (2017).
8. K. Latifi, H. Wijaya, Q. Zhou, Motion of Heavy Particles on a Submerged Chladni Plate. *Phys. Rev. Lett.* **122**, 184301 (2019).
9. A. Ozcelik, J. Rufo, F. Guo, Y. Gu, P. Li, J. Lata, T. J. Huang, Acoustic tweezers for the life sciences. *Nat. Methods* **15**, 1021–1028 (2018).
10. G. Destgeer, H. J. Sung, Recent advances in microfluidic actuation and micro-object manipulation via surface acoustic waves. *Lab Chip* **15**, 2722–2738 (2015).
11. M. Wu, A. Ozcelik, J. Rufo, Z. Wang, R. Fang, T. J. Huang, Acoustofluidic separation of cells and particles. *Microsyst. Nanoeng.* **5**, 32 (2019).
12. F. Petersson, L. Åberg, A.-M. Swärd-Nilsson, T. Laurell, Free flow acoustophoresis: Microfluidic-based mode of particle and cell separation. *Anal. Chem.* **79**, 5117–5123 (2007).
13. T. Franke, A. R. Abate, D. A. Weitz, A. Wixforth, Surface acoustic wave (SAW) directed droplet flow in microfluidics for PDMS devices. *Lab Chip* **9**, 2625–2627 (2009).
14. L. Y. Yeo, J. R. Friend, Ultrafast microfluidics using surface acoustic waves. *Biomicrofluidics* **3**, 12002 (2009).

15. F. Guo, Z. Mao, Y. Chen, Z. Xie, J. P. Lata, P. Li, L. Ren, J. Liu, J. Yang, M. Dao, S. Suresh, T. J. Huang, Three-dimensional manipulation of single cells using surface acoustic waves. *Proc. Natl. Acad. Sci.* **113**, 1522–1527 (2016).
16. M. Gedge, M. Hill, Acoustofluidics 17: Theory and applications of surface acoustic wave devices for particle manipulation. *Lab Chip* **12**, 2998–3007 (2012).
17. D. J. Collins, B. Morahan, J. Garcia-Bustos, C. Doerig, M. Plebanski, A. Neild, Two-dimensional single-cell patterning with one cell per well driven by surface acoustic waves. *Nat. Commun.* **6**, 8686 (2015).
18. J. Reboud, Y. Bourquin, R. Wilson, G. S. Pall, M. Jiwaji, A. R. Pitt, A. Graham, A. P. Waters, J. M. Cooper, Shaping acoustic fields as a toolset for microfluidic manipulations in diagnostic technologies. *Proc. Natl. Acad. Sci.* **109**, 15162–15167 (2012).
19. A. Marzo, M. Caleap, B. W. Drinkwater, Acoustic virtual vortices with tunable orbital angular momentum for trapping of mie particles. *Phys. Rev. Lett.* **120**, 044301 (2018).
20. L. Cox, K. Melde, A. Croxford, P. Fischer, B. W. Drinkwater, Acoustic Hologram Enhanced Phased Arrays for Ultrasonic Particle Manipulation. *Phys. Rev. Appl.* **12**, 064055 (2019).
21. Y. Li, X. Jiang, B. Liang, J. Cheng, L. Zhang, Metascreen-based acoustic passive phased array. *Phys. Rev. Appl.* **4**, 024003 (2015).
22. Z. Tian, S. Yang, P.-H. Huang, Z. Wang, P. Zhang, Y. Gu, H. Bachman, C. Chen, M. Wu, Y. Xie, T. J. Huang, Wave number--spiral acoustic tweezers for dynamic and reconfigurable manipulation of particles and cells. *Sci. Adv.* **5**, eaau6062 (2019).
23. Z. Tian, C. Shen, J. Li, E. Reit, H. Bachman, J. E. S. Socolar, S. A. Cummer, T. J. Huang, Dispersion tuning and route reconfiguration of acoustic waves in valley topological phononic crystals. *Nat. Commun.* **11**, 762 (2020).
24. M. Wiklund, R. Green, M. Ohlin, Acoustofluidics 14: Applications of acoustic streaming in microfluidic devices. *Lab Chip* **12**, 2438–2451 (2012).
25. J. S. Bach, H. Bruus, Bulk-driven acoustic streaming at resonance in closed microcavities. *Phys. Rev. E* **100**, 023104 (2019).
26. N. Nama, P.-H. Huang, T. J. Huang, F. Costanzo, Investigation of acoustic streaming patterns around oscillating sharp edges. *Lab Chip* **14**, 2824–2836 (2014).

27. D. J. Collins, Z. Ma, Y. Ai, Highly localized acoustic streaming and size-selective submicrometer particle concentration using high frequency microscale focused acoustic fields. *Anal. Chem.* **88**, 5513–5522 (2016).
28. D. J. Collins, Z. Ma, J. Han, Y. Ai, Continuous micro-vortex-based nanoparticle manipulation via focused surface acoustic waves. *Lab Chip* **17**, 91–103 (2017).
29. D. Ahmed, A. Ozcelik, N. Bojanala, N. Nama, A. Upadhyay, Y. Chen, W. Hanna-Rose, T. J. Huang, Rotational manipulation of single cells and organisms using acoustic waves. *Nat. Commun.* **7**, 11085 (2016).
30. Z. Mao, P. Li, M. Wu, H. Bachman, N. Mesyngier, X. Guo, S. Liu, F. Costanzo, T. J. Huang, Enriching nanoparticles via acoustofluidics. *ACS Nano* **11**, 603–612 (2017).
31. S. P. Zhang, J. Lata, C. Chen, J. Mai, F. Guo, Z. Tian, L. Ren, Z. Mao, P.-H. Huang, P. Li, S. Yang, T. J. Huang, Digital acoustofluidics enables contactless and programmable liquid handling. *Nat. Commun.* **9**, 2928 (2018).
32. P. Zhang, C. Chen, X. Su, J. Mai, Y. Gu, Z. Tian, H. Zhu, Z. Zhong, H. Fu, S. Yang, K. Chakrabarty, T. J. Huang, Acoustic streaming vortices enable contactless, digital control of droplets. *Sci. Adv.* **6**, eaba0606 (2020).
33. A. L. Facci, M. Porfiri, Analysis of three-dimensional effects in oscillating cantilevers immersed in viscous fluids. *J. Fluids Struct.* **38**, 205–222 (2013).
34. A. N. Nuriev, A. M. Kamalutdinov, A. G. Egorov, A numerical investigation of fluid flows induced by the oscillations of thin plates and evaluation of the associated hydrodynamic forces. *J. Fluid Mech.* **874**, 1057–1095 (2019).
35. K. Avila, D. Moxey, A. de Lozar, M. Avila, D. Barkley, B. Hof, The onset of turbulence in pipe flow. *Science* **333**, 192–196 (2011).
36. Q. Tang, J. Hu, S. Qian, X. Zhang, Eckart acoustic streaming in a heptagonal chamber by multiple acoustic transducers. *Microfluid. Nanofluid.* **21**, 28 (2017).
37. T. Freegarde, *Introduction to the Physics of Waves* (Cambridge Univ. Press, 2012).
38. R. Cao, B. Li, A simple and sensitive method for visual detection of heparin using positively-charged gold nanoparticles as colorimetric probes. *Chem. Commun.* **47**, 2865–2867 (2011).
39. X. Fu, L. Chen, J. Li, Ultrasensitive colorimetric detection of heparin based on self-assembly of gold nanoparticles on graphene oxide. *Analyst* **137**, 3653–3658 (2012).
40. K. D. McClatchey, *Clinical Laboratory Medicine* (Lippincott Williams & Wilkins, 2002).

41. L. E. Kinsler, A. R. Frey, A. B. Coppens, J. V Sanders, Fundamentals of acoustics, in *Fundam. Acoust. 4th Ed. by Lawrence E. Kinsler, Austin R. Frey, Alan B. Coppens, James V. Sanders, pp. 560. ISBN 0–471–84789-5. Wiley-VCH, December 1999.*, 560 (1999).
42. P. Hahn, I. Leibacher, T. Baasch, J. Dual, Numerical simulation of acoustofluidic manipulation by radiation forces and acoustic streaming for complex particles. *Lab Chip* **15**, 4302–4313 (2015).
43. J. Lei, P. Glynne-Jones, M. Hill, Acoustic streaming in the transducer plane in ultrasonic particle manipulation devices. *Lab Chip* **13**, 2133–2143 (2013).
44. G. G. Stokes, On the theories of the internal friction of fluids in motion, and of the equilibrium and motion of elastic solids. *Trans. Cambridge Philos. Soc.* **8** (1880).
45. Q. Tang, J. Hu, Diversity of acoustic streaming in a rectangular acoustofluidic field. *Ultrasonics* **58**, 27–34 (2015).
46. Q. Tang, J. Hu, Analyses of acoustic streaming field in the probe-liquid-substrate system for nanotrapping. *Microfluid. Nanofluid.* **19**, 1395–1408 (2015).
47. J. Lighthill, Acoustic streaming. *J. Sound Vib.* **61**, 391–418 (1978).
48. C. Devendran, I. Gralinski, A. Neild, Separation of particles using acoustic streaming and radiation forces in an open microfluidic channel. *Microfluid. Nanofluid.* **17**, 879–890 (2014).
49. D. W. Moore, P. G. Saffman, The motion of a vortex filament with axial flow. *Philos. Trans. R. Soc. A* **272**, 403–429 (1972).